Heterogeneous fractionation profiles of meta-analytic coactivation networks

Angela R. Laird[1], Michael C. Riedel[1], Mershack Okoe[2], Radu Jianu[2], Kimberly L. Ray[3], Simon B. Eickhoff[4,5],
Stephen M. Smith[6], Peter T. Fox[7,8,9], Matthew T. Sutherland[10]

[1]Department of Physics, Florida International University, Miami, FL
[2]School of Computing and Information Sciences, Florida International University, Miami, FL
[3]Research Imaging Center, University of California Davis, Sacramento, CA, USA
[4]Institute of Clinical Neuroscience and Medical Psychology, Heinrich-Heine University, Düsseldorf, Germany
[5]Institute of Neuroscience and Medicine, Research Center Jülich, Jülich, Germany
[6]Oxford Centre for Functional MRI of the Brain, University of Oxford, Oxford, UK
[7]Research Imaging Institute, University of Texas Health Science Center, San Antonio, TX, USA
[8]Research Service, South Texas Veterans Administration Medical Center, San Antonio, TX, USA
[9]State Key Laboratory for Brain and Cognitive Sciences, University of Hong Kong
[10]Department of Psychology, Florida International University, Miami, FL

__Corresponding Author__
Dr. Angela R. Laird, Ph.D.
Professor, Department of Physics, AHC4 310
Florida International University
Modesto Maidique Campus
11200 SW 8th Street
Miami, FL 33199
305.348.6737 (phone)
305.348.6700 (fax)
alaird@fiu.edu

Keywords: neuroimaging meta-analysis, independent component analysis, meta-analytic connectivity modeling, meta-analytic coactivation networks, BrainMap, fractionation, neuroinformatics

Abstract

Computational cognitive neuroimaging approaches can be leveraged to characterize the hierarchical organization of distributed, functionally specialized networks in the human brain. To this end, we performed large-scale mining across the BrainMap database of coordinate-based activation locations from over 10,000 task-based experiments. Meta-analytic coactivation networks were identified by jointly applying independent component analysis (ICA) and meta-analytic connectivity modeling (MACM) across a wide range of model orders (i.e., d = 20 to 300). We then iteratively computed pairwise correlation coefficients for consecutive model orders to compare spatial network topologies, ultimately yielding fractionation profiles delineating how "*parent*" functional brain systems decompose into constituent "*child*" sub-networks. Fractionation profiles differed dramatically across canonical networks: some exhibited complex and extensive fractionation into a large number of sub-networks across the full range of model orders, whereas others exhibited little to no decomposition as model order increased. Hierarchical clustering was applied to evaluate this heterogeneity, yielding three distinct groups of network fractionation profiles: high, moderate, and low fractionation. BrainMap-based functional decoding of resultant coactivation networks revealed a multi-domain association regardless of fractionation complexity. Rather than emphasize a cognitive-motor-perceptual gradient, these outcomes suggest the importance of inter-lobar connectivity in functional brain organization. We conclude that high fractionation networks are complex and comprised of many constituent sub-networks reflecting long-range, inter-lobar connectivity, particularly in fronto-parietal regions. In contrast, low fractionation networks may reflect persistent and stable networks that are more internally coherent and exhibit reduced inter-lobar communication.

Introduction

Enhanced insight into the network-level functional organization of the human brain may provide a more complete and coherent framework to appreciate the spectrum of human mental abilities. For example, functional connectivity analyses utilizing multivariate independent component analysis (ICA) have characterized the spatial topography of consistently identified brain networks in resting state functional magnetic resonance imaging (rs-fMRI) data (Beckmann, 2012; Calhoun and Adali, 2012). ICA-derived resting state networks (Beckmann et al., 2005; De Luca et al., 2006) extend across anatomically distributed regions, are consistent across studies (Damoiseaux et al., 2006; Zuo et al., 2010) and species (Wey et al., 2014; Vincent et al., 2007; Moeller et al., 2009), and reliably define functional neural systems, such as the default mode (Raichle et al., 2001), perceptual (e.g., visual or auditory), sensorimotor (e.g., motor-hand, motor-speech, premotor), and high-level cognitive networks (e.g., unilateral and bilateral fronto-parietal regions associated with memory, language, and central executive function) (Damoiseaux et al., 2006; Kiviniemi et al., 2009; Biswal et al., 2010; Allen et al., 2011). We previously demonstrated that this network-based architecture persists across both resting and task states, as shown in a database-driven meta-analysis from thousands of task conditions (Smith et al., 2009). Using ICA, a primary set of activation networks was identified, which represented the major modes of co-occurrence across the diverse range of activations reported in the literature. Subsequently, we reported a novel approach in connectome discovery science in which ICA and pattern classification techniques were jointly applied to characterize the functional similarity across meta-analytic networks (Laird et al., 2011a). Using this approach, we identified four groupings of the major coactivation networks with similar behavioral properties across studies: (a) motor and visuospatial integration, coordination, and execution, (b) visual processing, (c) emotion and interoceptive processing, and (d) higher cognition. Networks in the first three functional groups exhibited strongly thematic functional properties, whereas the fourth group was associated with a divergent set of properties that differed across networks, yet all involved high-level cognitive processing.

While the spatial topographies of these canonical neural systems have been consistently observed across studies, it is unclear how this functional architecture translates across different scales. Indeed, although *multivariate* analyses of fMRI data have become commonplace, such analyses are typically not yet *multi-scale*. Evidence from graph theory approaches (Bullmore and Sporns, 2009) suggests that the brain follows a modular organization, with communication hubs (Achard et al., 2006; Hagmann et al., 2008; Buckner et al., 2009) and properties similar to those of small-world networks (Salvador et al., 2005; Meunier et al., 2009; He et al., 2009). However, there remains much to be understood regarding the fractionation scheme that defines how large-scale core systems are decomposed into sub-systems. ICA is typically performed at a pre-selected model order *d* (e.g., generally, a low order/scale of 20-40 components), rather than across multiple scales. Although prior work has sought to develop analytic strategies for automatically identifying an optimal model order of interest (Beckmann and Smith, 2004; Himberg et al., 2004; Li et al., 2007; Ray et al., 2013), these methods are somewhat arbitrary and usually depend upon a number of factors (e.g., field strength, number of time points, number of subjects, and data quality). A recent study established the importance of this dimensionality parameter (Wang and Li, 2015), demonstrating that the number of components can critically affect ICA results. Only a few studies have directly compared ICA-based resting state networks across different model orders (Smith et al., 2009; Kiviniemi et al., 2009; Abou-Elseoud et al., 2010; Pamilo et al., 2012), suggesting a hierarchical network structure (i.e., the 20 networks observed at a low-dimensionality ICA can be decomposed into distinct sub-networks at a model order of 70). However, no study has yet synthesized the dynamic nature of these networks by scaling across a wide range of model orders.

In a previous study, we examined meta-analytic task co-occurrence networks across multiple model orders using the BrainMap database, and demonstrated a model order of 20 components provides an optimal decomposition for low model order ICA, while 70 components is optimal for higher model orders (Ray et al., 2013). Although multiple model orders were analyzed, our results did not include an integrative assessment of the decomposition trajectories across all model orders, for all networks. Here, we more fully explored how large-scale distributed meta-analytic coactivation networks fractionate into smaller sub-networks and/or individual nodes using a multivariate, multi-scale analysis. The emphasis of the present study is not on a single model order, nor is it our objective to propose that higher model orders are more or less meaningful than lower model orders. Rather, we sought to characterize meta-analytic coactivation networks from a wider lens and evaluate the dynamic range of fractionation profiles across many model orders. To this end, we leveraged two complementary neuroimaging meta-analytic techniques to examine how "*parent*" functional brain systems can be decomposed into constituent "*child*" sub-networks, thereby providing insight into the fractionation properties of functional brain architecture. First, we applied ICA using a range of model orders to a database of task-based activations reported in the literature. Second, we applied meta-analytic connectivity modeling (MACM; Laird et al., 2009a; Robinson et al., 2010; Eickhoff et al., 2010) to the resultant ICA components to identify a set of large-scale coactivation networks at each model order. Meta-analytic coactivation networks are derived from activation patterns reported across a range of experimental neuroimaging tasks and paradigms, are complementary to seed-based resting state correlations, and have been validated in a series of papers comparing findings to other network mapping techniques (Robinson et al., 2010; 2012; Eickhoff et al., 2010; 2011; Narayana et al., 2012; Jakobs et al., 2012; Reetz et al., 2012). Pairwise correlation matrices quantifying the similarity between networks at sequential dimensionalities were calculated to construct fractionation profiles describing how the parent networks were decomposed into child sub-networks. Consistent with and extending our previous work, we hypothesized that *perceptual and motor* parent networks would yield simple fractionation profiles with relatively few numbers of child sub-networks. Conversely, we additionally hypothesized that *cognitive* parent networks would yield complex fractionation profiles with relatively large numbers of child sub-networks. We observed that the fractionation profiles differed dramatically across canonical networks, with some exhibiting complex fractionation into a large number of sub-networks and others exhibiting little to no decomposition. Hierarchical clustering of the heterogeneous fractionation profiles allowed us to then classify networks into three distinct groups: high fractionation, moderate fractionation, and low fractionation. Our results demonstrate that varying model order provides enhanced insight into the heterogeneous fractionation profiles of meta-analytic coactivation networks.

Methods

Independent Component Analysis of the BrainMap Database

Following procedures established in our prior work, meta-analysis was carried out using data archived in the BrainMap database (http://brainmap.org; Fox and Lancaster, 2002; Laird et al., 2005a; 2009b; 2011b). Peak coordinates were extracted from 10,899 neuroimaging experiments representing activation locations observed among 100,861 healthy participants across a wide range of behavioral task conditions. Experiments were filtered to exclude patient populations, thereby mitigating potential bias due to effects of disease or treatment effects. Coordinates reported in MNI space (Evans et al., 1993; Collins et al., 1994) were converted into Talairach space (Talairach and Tournoux, 1988) using the Lancaster transformation (Lancaster et al., 2007), reducing spatial disparity across normalization templates (Laird et al., 2010). The coordinates were then modeled with a three-dimensional Gaussian probability distribution reflecting the spatial uncertainty of each focus based on an estimation of the inter-subject and inter-laboratory variability typically observed in neuroimaging experiments, weighted by the number of subjects included in each experiment (Eickhoff et al., 2009). This algorithm limits the meta-analysis to an anatomically constrained space specified by a grey matter mask, and includes a method that calculates the above-chance clustering between experiments (i.e., random-effects analysis), rather than between foci (i.e., fixed-effects analysis), and also accounts for differences in sample sizes across included studies (Eickhoff et al., 2009). The probabilities of all foci reported in a given experiment were computed, resulting in a modeled activation (MA) map for each experiment (Figure 1, Step 1). The per-experiment MA probability maps were converted into feature vectors of voxel values and concatenated horizontally to form an array of size *n=10,899* experiments by *v* voxels. The spatial resolution of the images was 2mm x 2mm x 2mm, and v was equal to 226,654 voxels.

Spatial ICA at a model order of *d* was applied to these data using FSL's MELODIC (multivariate exploratory linear optimized decomposition into independent components; Beckmann et al., 2005) to decompose the MA maps into *d* spatiotemporal components (FMRIB Software Library; Smith et al., 2004; Woolrich et al., 2009; Jenkinson et al., 2012) (Figure 1, Step 2). This approach has been used in previous meta-analytic ICA studies at dimensionalities of *d* = 20 (Laird et al., 2011a; Smith et al., 2009), as well as ranging from *d* = 20-200 at intervals of 10 (Ray et al., 2013). Increasing ICA dimensionality yields increasingly smaller brain regions exhibiting increasingly higher average component z-score values (Abou-Elseoud et al., 2010; Ray et al., 2013). Here, we performed ICA multiple times (*t* = 29) to extract sets of *d* = 20 – 300 independent components at intervals of 10, and thereby characterized a greater range of model orders than has previously been assessed. Thus, ICA was performed at 29 different model orders each with *d* components, yielding a cumulative total of 4,640 components. At each model order, ICA maps were converted to *z* statistic images via a normalized mixture model fit and viewed on a Talairach space template image (Kochunov et al., 2002). A threshold of *z* > 4 was selected to provide methodological consistency to prior BrainMap-based studies of ICA component maps (Smith et al., 2009; Laird et al., 2011; Ray et al., 2013).

Generation of Meta-Analytic Coactivation Networks

ICA-derived spatially independent components are known to be consistent, and have been reported in a host of rs-fMRI publications and in task-based BrainMap meta-analytic coactivation studies (Smith et al., 2009; Laird et al., 2011; Ray et al., 2013). At a low model order (e.g., 20-40), the broad spatial patterns of the observed components are easily recognizable (e.g., default mode, medial visual, salience, etc.); however, some variations are commonly observed in the extent of the primary clusters, as well as the absence or presence of smaller, secondary clusters. Given this variability, we sought to identify a more extensive and complete definition of the functional brain networks underlying each of the ICA component images. Thus, to more fully identify large-scale meta-analytic coactivation networks, we performed meta-analytic connectivity modeling (MACM) on the ICA-derived component images from each model order (Figure 1, Step 3). That is, this two-step strategy was chosen to first identify the spatially independent networks using ICA and subsequently apply MACM to refine and strengthen the ICA results. The MACM approach examines coactivations for a user-defined region of interest and yields images of task-based connectivity (Laird et al., 2009a; Robinson et al., 2010; Eickhoff et al., 2010). Thresholded component images across all model orders served as seeds in the BrainMap database to identify brain areas that were coactivated with voxels in each component map. Specifically, the BrainMap database was queried for all experiments that reported one or more activation coordinates within the spatial boundaries delineated by each ICA spatial map. Search results were limited to coordinates of brain activations (i.e., no deactivations) reported in studies of healthy participants. The whole-brain coactivation coordinates were extracted along with the corresponding metadata from the BrainMap taxonomy (Fox et al., 2005), which characterize the experimental design, including paradigm class and behavioral domain, for each experimental contrast.

Once the whole-brain coactivation coordinates were identified for each thresholded component, the activation likelihood estimation (ALE) method was used to perform MACM, yielding a meta-analytic image representing the above-chance probability that a given voxel coactivated with the component seed map. In MACM, an ALE score is calculated at every voxel in the brain (Turkeltaub et al., 2002; Laird et al., 2005b; Eickhoff et al., 2009; Turkeltaub et al., 2012; Eickhoff et al., 2012), and these ALE scores are transformed to P values to identify locations with significantly higher ALE scores than an empirically derived null distribution. Each ALE map was thresholded at a false discovery rate (FDR) threshold of $P < 0.05$ with a minimum cluster size of 250 mm^3. This procedure yielded a statistically significant MACM map delineating whole-brain meta-analytic coactivation networks for each of the 4,640 ICA component images across.

Fractionation Profiles: Spatial Correlations Across Model Orders

After generating the meta-analytic coactivation networks across all model orders, we sought to establish a hierarchical framework of network fractionation profiles. At the lowest model order, 20 coactivation networks were obtained, representing the major modes of functional activation observed during task performance, which corresponded to the networks of correlated spontaneous fluctuations observed during the resting state (Smith et al., 2009). Given the high reproducibility of these canonical networks across multiple studies, we then aimed to characterize how these networks fractionate into sub-networks as a function of increasing model order. To this end, we utilized the Pearson correlation coefficient. The procedure began by first masking each unthresholded MACM image to include only those voxels in the Talairach brain mask (Kochunov et al., 2002). Then, each MACM was reduced from a three-dimensional matrix to a one-dimensional array, where the length of the array was equal to the number of voxels in the brain mask (i.e., same size for all images). The one-dimensional array corresponding to a single model order was computed for every model order *d*; the results were subsequently concatenated to generate a *d* x *v* matrix. Next, we computed the Pearson correlation coefficients between network pairs obtained at model orders 20 and 30, and assigned each child network observed at model order 30 to a single parent network at model order 20 based on the highest observed correlation coefficients. A high correlation coefficient indicated a strong correspondence between spatial topographies across adjacent model orders. By evaluating the highest coefficient at d = 30 and assigning to the corresponding parent at d = 20, we allowed for multiple child networks to be assigned to a given parent (i.e., since 30 > 20), thereby indicating potential fractionation of a single parent network into multiple child sub-networks. Next, to establish the second level of hierarchical organization, we computed the correlations between network pairs at model orders 30 and 40. This step-wise procedure was iteratively repeated for all consecutive model order pairings *i* and *i+10*, yielding a hierarchical assembly of parent-child assignments in which the sub-networks at successive model orders were assigned to a given parent network at the previous model order. The results yielded a *d* x *d+10* matrix of correlation coefficients (Figure 1, Step 4). In this way, the hierarchical parent-child assignments from all model orders allowed us to assign all 4,640 child sub-networks and ultimately construct network fractionation profiles delineating how each of the 20 canonical coactivation networks were fractionated. Importantly, if the relative difference between correlations of model order pairings was found to be within 10% of the average observed difference between highest and second-highest correlations, a child was assigned to multiple parents. This was implemented to account for scenarios in which a child sub-network may potentially “belong” to multiple parent networks (see Supplemental Material for more details).

We anticipated a wide range of different fractionation profiles for the 20 canonical coactivation networks, in accordance with our hypotheses that low-level perceptual and motor coactivation networks would fractionate into a relatively small number of sub-networks, whereas high-level cognitive coactivation networks would fractionate into a relatively high number of sub-networks. To evaluate the heterogeneity of the fractionation profiles for the 20 canonical coactivation networks, we generated an n X t array, where n refers to the n = 20 canonical networks and t refers to the 29 model orders (i.e., from 20 to 300 in intervals of 10). Each value of the array indicated the number of fractionated child sub-networks observed at a given model order. The 20 canonical networks were subsequently grouped into clusters by applying hierarchical clustering analysis to this array using the *average* linkage algorithm and the *euclidean* distance metric (Laird et al., 2011a; Laird et al., 2015) (Figure 1, Step 5). Given the small number of variables, we identified a clustering solution using simple visual inspection of the resultant dendrogram.

Functional Decoding of Meta-Analytic Coactivation Networks

We also evaluated the functional properties of the observed meta-analytic coactivation networks across multiple model orders. Experiments in the BrainMap database have been manually annotated with metadata that describe the experimental design of each archived study. This metadata includes the "*behavioral domain*", which classifies the mental function isolated by the experimental contrast. There are five main levels of behavioral domain classification: action, cognition, emotion, interoception, and perception. A complete description of the BrainMap metadata taxonomy, along with a comprehensive list of behavioral domains is available at http://brainmap.org/taxonomy. We analyzed the per-experiment behavioral domain annotations to determine the mental functions that were most likely to contribute to the observed coactivation networks. Forward and reverse inference analyses (Poldrack, 2006; Yarkoni et al., 2011) were performed on the distributions of behavioral domains for each coactivation network to determine over-representation compared to the entire BrainMap database (Cieslik et al., 2013; Nickl-Jockschat et al., 2015). Forward inference is the probability of observing activity in a brain region given knowledge of the psychological process, whereas reverse inference is the likelihood that a given metadata term resulted in an activation within a network. In the forward inference approach, we tested whether the conditional probability of activation given a particular label [P(Activation|Domain)] was higher than the baseline probability of activating the region in question per se [P(Activation)]. Significance was established using a binomial test ($P < 0.05$, corrected for multiple comparisons using Bonferroni's method), which was appropriate since our goal was to compare the observed distribution to the expected distribution given only two categories (i.e., frequency of term within a network and across the entire database). In the reverse inference approach, we identified the most likely behavioral domain given activation in a particular network. This likelihood P(Domain|Activation) can be derived from P(Activation|Domain) as well as P(Domain) and P(Activation) using Bayes rule. Significance ($P < 0.05$, corrected for multiple comparisons using Bonferroni's method) was then assessed by means of a chi-squared test.

Results

Generation of Meta-Analytic Coactivation Networks

ICA was applied at 29 dimensionalities (*d* = 20 to 300 in intervals of 10) to over 10,899 modeled experiment images archived in the BrainMap database. For the resultant ICA spatial components, the average number of significant voxels ($z > 4$) per component exhibited a logarithmic decrease with model order ($R^2 = 0.972$) (Figure 2, green) while the average *z*-score per component increased linearly ($R^2 = 0.990$) (not shown), in agreement with prior work (Abou-Elseoud et al., 2010; Ray et al., 2013). Meta-analytic connectivity modeling (MACM) was performed on each of the resultant 4,640 ICA maps, yielding meta-analytic coactivation networks. For the MACM-based coactivation networks, the average number of significant voxels per MACM exhibited a linear decrease with model order ($R^2 = 0.977$) (Figure 2, blue). As model order increased, both the ICA components and the MACM-based coactivation network maps exhibited a shift from broad, spatially extended networks encompassing multiple brain regions to smaller and more localized individualized sub-networks and/or nodes. At *d* = 20, the mean ICA component whole-brain volume was 109,381 mm^3 (*sd* = 45,111 mm^3) and the mean MACM-based coactivation network volume was 335,446 mm^3 (*sd* = 65,750 mm^3). In contrast, at *d* = 300, the mean ICA component whole-brain volume decreased to 24,240 mm^3 (*sd* = 4,696 mm^3) and the mean MACM-based coactivation networks volume decreased to 255,748 mm^3 (*sd* = 52,645 mm^3). Notably, the relative difference was such that the ICA components decreased in volume across model order at a greater rate than did the MACM maps. Moreover, these data illustrate that in comparison to the ICA component maps, the MACM-based coactivation networks captured a more large-scale and widely distributed spatial topology, with an average volume across all model orders greater than six times as large (i.e., the ICA component images had an average volume of 43,383 mm^3 across all model orders whereas the larger MACM coactivation networks had an average volume of 289,361 mm^3).

At the lowest model order, 20 canonical coactivation networks were obtained, representing the major modes of functional activation exhibited by the brain over a range of tasks. Multiple prior ICA studies (Damoiseaux et al., 2006; Smith et al., 2009; Zuo et al., 2010; Laird et al., 2011a; Allen et al., 2011; Wisner et al., 2013) have consistently reported these networks, including the: **dorsal attention network**, which is localized to dorsal fronto-parietal regions, such as the frontal eye fields and intraparietal sulci (Corbetta and Shulman, 2002; Fox et al., 2006; Dosenbach et al., 2006); **left- and right-lateralized central executive networks** in dorsolateral prefrontal and posterior parietal cortices (Vincent et al., 2008; Sridharan et al., 2008); **salience network** in the anterior insula and anterior cingulate cortices (Seeley et al., 2007; Menon and Uddin, 2010); **anterior and poster default mode networks**, including dorsomedial prefrontal cortices, posterior cingulate, and precuneus (Raichle et al., 2001; Buckner et al., 2008); **self-referential network** in ventromedial prefrontal cortices (Mantini et al., 2007); **visuomotor coordination network** in medial premotor and supplementary motor areas; **hand sensorimotor network** in bilateral hand areas of the somatosensory and motor cortices; **mouth sensorimotor network** in bilateral face and mouth areas of the somatosensory and motor cortices; **posterior association network** in the medial posterior parietal association area of the superior parietal lobule (Scheperjans et al., 2005); **auditory network** in primary and secondary auditory cortices located in bilateral superior temporal gyri (Seifritz et al., 2002); **medial and lateral visual networks** in striate and extrastriate visual cortices; **visual association network** in middle temporal visual association areas at the temporo-occipital junction; **contextual association network** (Bar et al., 2008; Sulpizio et al., 2013), which is most commonly associated with processing of scenes and places and includes retrosplenial cortex and lingual gyri (Henderson et al., 2007; Chai et al., 2010); **temporo-limbic network** including amygdala and parahippocampal gyri, **basal ganglia and thalamus network** (Robinson et al., 2009; Kim et al., 2013); and **cerebellum network** (Dobromyslin et al., 2012). In addition, one artifactual component was observed, which was disregarded, and all subsequent analyses proceeded with 19 canonical coactivation networks. In BrainMap-based ICA analyses, noise components are not observed due to artifacts such as movement, physiological noise, or CSF partial volume, but instead are thought to correspond to coordinate-based template mismatch errors (Laird et al., 2011a).

Heterogeneity of Network Fractionation Profiles

After generating the MACM-based coactivation networks, we constructed fractionation profiles by iteratively evaluating the parent-child assignments of these networks across consecutive model orders, starting from the observed spatial correlation between networks at model orders 20 and 30. Parent-child assignments were determined for each of the canonical coactivation networks observed at the lowest model order by following them through the full range of model orders. When comparing d = 30 to d = 20 networks, the mean assigned correlation coefficient value was 0.909 (sd = 0.066), whereas the mean assigned correlation value when comparing d = 290 to d = 300 was 0.925 (sd = 0.059). Across all pairwise model order comparisons (e.g., 20x30, 30x40, …, 290x300), the average mean assigned correlation value was 0.928 (sd = 0.066), with a minimum of 0.648 and maximum of 0.996. There were 4,620 assignments made from model order 20 to 300, assuming a child sub-network was matched to only a single parent network (i.e., highest correlation assignment only). We computed the number of times in which the correlations between the child and potential parents were observed to be within 0.01

of the highest correlation and found that to occur for 312 assignments, or 6.3% of the total. These 312 child networks were assigned to multiple parent networks, yielding an overall sum of 4,932 parent-child assignments across the entire analysis.

Once the pairwise parent-child assignments were computed, each sub-network at d = 30 and higher was matched to its corresponding canonical coactivation network at d = 20. Based on these assignments, we observed that the number of child sub-networks assigned to each of the canonical networks varied considerably across the canonical networks. For example, at d = 300, a mean of 26.95 sub-network assignments were made to each canonical network (*sd* = 21.31; *max* = 58; *min* = 0), i.e., on average, 26.95 of the d = 300 networks were assigned to each of the d = 20 canonical networks. Figure 3 depicts the number of child sub-networks observed at each model order for the canonical parent networks. Thus, the observed fractionation profiles differed dramatically across canonical networks: some networks exhibited complex and extensive fractionation into a large number of sub-networks across the full range of model orders, whereas others exhibited little to no decomposition as model order increased. Given this variability across networks, we performed hierarchical clustering analysis on the n X t array of values indicating the number of fractionated child sub-networks observed at a given model order, where n = 19 canonical networks and t = 29 different model orders. Hierarchical clustering using the *average* linkage and *euclidean* distance yielded a simple dendrogram in which three clusters were visually observed (Figure 3, inset). Accordingly, clustering analysis demonstrated that the overall fractionation of systems into sub-systems could be categorized into three groups: high fractionation, moderate fractionation, and low fractionation.

The three-cluster solution shown in Figure 3 (inset) forms the basis for the network groupings provided in Figures 4, 5, and 6, which illustrate the spatial topography of the canonical coactivation networks (top row), along with the corresponding fractionation profiles for high, moderate, and low fractionation patterns (middle row), respectively. Within the spatial maps, the black contour lines define the ICA component (seed) images, while the more extensive transparent spectrum color map defines the MACM-based coactivation networks. Within the fractionation profiles, the pattern of child assignments for the canonical networks across all model orders is visualized as a set of hierarchical layouts using Cytoscape version 3.2.0 (Shannon et al., 2003). A single element (i.e., straight line) of each profile plot corresponds to a sub-network observed at a given model order, which is distinguished by a color gradient (e.g., from light blue at d=20 to light green at d=300, etc.). Child networks from consecutive model orders are situated adjacent to each other. Gray lines connecting elements indicate a decomposition branch with extensive fractionation of networks, necessitating a larger spatial allocation for visualization (i.e., these lines do not indicate dissimilarity). Large connective arcs are indicative of shared networks at higher model orders between two distinct decomposition branches. Notably, the profiles shown in Figure 4 (Networks 1-7) exhibit high fractionation with extensive and complex decomposition of the selected canonical networks into many child sub-networks. For example, the right-lateralized central executive network (Figure 4, Network 1), comprising right dorsolateral prefrontal and posterior parietal regions, displayed the highest degree of fractionation with 58 constituent components at model order 300. The dorsal attention (Network 2), hand sensorimotor (Network 3), cerebellar (Network 4), salience (Network 5), basal ganglia and thalamus (Network 6), visuomotor coordination (Network 7), visual association (Network 8), and mouth sensorimotor (Network 9) networks also exhibited high fractionation patterns, in order of decreasing profile complexity. In contrast, the patterns in Figure 5 (Networks 10-12) are simpler, with fewer sub-networks and less branching. These moderate fractionation profiles included the lateral visual (Network 10), left-lateralized central executive (Network 11), and temporo-limbic (Network 12) networks. Lastly, the profiles in Figure 6 (Networks 13-19) exhibited little to no fractionation into sub-networks, but instead suggested that these canonical networks were stable and persistent across model orders. Low fractionation networks included the auditory (Network 13), posterior default mode (Network 14), medial visual (Network 15), anterior default mode (Network 16), contextual association (Network 17), self-referential (Network 18), and posterior association (Network 19) networks.

Functional Decoding of Meta-Analytic Coactivation Networks

Forward and reverse inference analyses were carried out on the BrainMap behavioral domains associated with experiments contributing to each meta-analytic coactivation network to characterize their associated mental processes. The significant behavioral domains observed at both the lowest and highest model orders (i.e., d = 20 and 300) are visualized in Figures 4, 5, 6 (bottom row), providing a summary of how mental processes vary from canonical brain networks (d = 20) to constituent fractionated sub-networks (d = 300). The mean number of significant domains across all networks was 15.05 at d = 20 and 13.51 at d = 300; an average of 13.97 significant domains per component was observed across all model orders. This variable distribution of significant behavioral domains is visualized as set of attribute circle layouts using Cytoscape (Shannon et al., 2003). Here, the five categories of BrainMap behavioral domains are represented by different colors at the periphery of the circle: “Action” (red), “Cognition” (green), “Emotion” (blue), “Interoception” (yellow), and “Perception” (magenta). Individual colored squares at the periphery of each circle correspond to the sub-categories within a given behavioral domain (see http://brainmap.org/taxonomy for a complete list). Two types of shapes are viewed inside each circular plot: a large white diamond representing the results at $d = 20$ and smaller gray circles representing the results at $d = 300$. Note that more complex fractionation profiles in Figure 4 yield an increased number of sub-networks (i.e., more gray circles) as compared to less complex fractionation profiles with fewer sub-networks in Figures 5 and 6. Colored lines extending from the white diamond and gray circles indicate significant behavioral domains (and sub-domains) corresponding to the networks at $d = 20$ and 300, respectively; the spatial location of the diamond and circles within each plot illustrates the strength of correspondence. For example, the posterior default mode network in Figure 6 (Network 14) is associated with multiple behavioral sub-domains at $d = 20$, but it is located spatially closer to “Cognition” (green lines), emphasizing this network’s weighting toward cognitive processes (e.g., social cognition and autobiographical memory).

Figure 4 reveals that the highly fractionated networks demonstrated a complex and widespread distribution across a range of behavioral domains, corresponding to an association with numerous mental processes. Other networks shown in Figures 5 and 6, while still exhibiting recruitment across multiple domains, displayed a less complex profile, exhibiting significant association with only a few behavioral states. Importantly, the behavioral profiles shown in Figures 4, 5, and 6 exhibit at least one significant association with all five behavioral domains at model order 300, indicating fractionation into a diverse range of networks that recruit across multiple mental states regardless of high, moderate, or low fractionation profiles. The only exception to this was observed for the self-referential network (Figure 6, Network 18), which demonstrated a simple, one-dimensional fractionation profile and was associated with the behavioral domains of Cognition, Emotion, Interoception, and Perception, but not Action (red).

Visualization Environment

The meta-analytic coactivation networks and corresponding functional decoding results can be explored in an online visualization environment: http://vizlab.cs.fiu.edu/brainvis. This visualization maps the fractionation of the observed meta-analytic coactivation networks across a limited number of exemplar model orders, e.g., $d = 20$, 30, 70, and 120, within a single zoomable and pannable view. The networks are depicted as 2D point-glyphs and fractionation is explicitly shown by visual links spanning lower to higher order networks. Network glyphs are augmented by small icons indicating coronal network views, making networks easily recognizable within a reduced space. Selection of individual networks allows users to expand to show higher resolution network images along all three projection planes in a connected view. In addition, the visualization explicitly embeds functional decoding results (i.e., behavioral domain terms) within the same space using visual links with a salience directly proportional to the strength of the correlation. The unified 2D layout of meta-analytic coactivation networks and behavioral terms is optimized to group together fractionating components and behavioral terms that they link to, thus revealing clusters of structurally and behaviorally related data. The visualization relies on data driven documents (D3) (Bostock et al., 2011) to render itself into regular browsers and provide advanced interaction capabilities.

Discussion

We jointly applied independent component analysis (ICA) and meta-analytic connectivity modeling (MACM) across a range of model orders to BrainMap coordinate-based data to derive meta-analytic coactivation networks. In contrast to ICA alone, this joint ICA-MACM approach allowed a richer characterization of sub-network architecture across a wider range of model orders than previously described (i.e., $d = 20$ to 300). Pairwise correlation matrices quantifying the similarity between networks at sequential dimensionalities were calculated to construct fractionation profiles describing how the canonical "*parent*" networks were decomposed into constituent "*child*" sub-networks. The observed fractionation profiles differed dramatically across canonical networks, with some exhibiting complex fractionation into a large number of sub-networks and others exhibiting little to no decomposition. Hierarchical clustering of the heterogeneous fractionation profiles allowed us to classify networks into three distinct groups: high fractionation, moderate fractionation, and low fractionation. These outcomes provide insight into the functional architecture of the human brain.

Our hypothesis that low-level perceptual and motor networks would yield simple fractionation profiles with relatively few numbers of child sub-networks while high-level cognitive networks would yield complex fractionation profiles with relatively large numbers of child sub-networks was partially supported, in agreement with prior work (Ding et al., 2011). As shown in the bottom rows of Figures 4-6, many of the high fractionation networks emphasized cognitive behavioral domains (green lines), while many of the low fractionation networks did not. Of the high fractionation networks, the right central executive (Figure 4, Network 1), dorsal attention (Network 2), salience (Network 5), and visuomotor coordination (Network 7) networks all demonstrated strong cognitive roles and exhibited high fractionation patterns. Specifically, both the dorsal attention and central executive networks recruit across bilateral frontal and parietal regions and are known to be involved in coordinating externally directed attentional resources and management of highly adaptive control processes, respectively (Corbetta and Shulman, 2002; Fox et al., 2006; Dosenbach et al., 2006; Vincent et al., 2008; Sridharan et al., 2008). Similarly, the salience and visuomotor coordination networks are responsible for orienting between external stimuli and internal events (Seeley et al., 2007; Menon and Uddin, 2010) and cognitive control of visuomotor timing and preparation of executed movements (Laird et al., 2011a), respectively. Moreover, the cerebellar (Network 4) and basal ganglia/thalamus (Network 6) networks were observed in the high fractionation group: these networks are known to be highly heterogeneous and have been observed to activate across a wide range of cognitive paradigms (Robinson et al., 2009; Kim et al., 2013; Dobromyslin et al., 2012; Riedel et al., 2015).

In contrast, multiple perceptual networks demonstrated low to moderate fractionation patterns (Figures 5 and 6), including the auditory (Network 13) and medial and lateral visual (Networks 15 and 10). The contextual association network (Network 17), which is commonly associated with perception of scenes and places (Henderson et al., 2007; Chai et al., 2010) and is more broadly responsible for contextual processing (Bar et al., 2008; Sulpizio et al., 2013), persisted intact across many model orders, but fractionated into three sub-networks at model order d = 270: anterior, with corresponding parietal coactivations; posterior with occipital coactivations; and inferior, with cerebellar coactivations (Baldassano et al., 2013). The posterior parietal association network (Network 19) in medial superior parietal lobule (Scheperjans et al., 2005), associated with higher somatosensory perception of egocentric space (Parkinson et al., 2010; Lester and Dassonville, 2014; Land, 2014), was not observed subsequent to d = 30, and thus exhibited no further correlations. Beyond d = 30, the posterior parietal association network was subsumed by the hand sensorimotor network (Network 3) and incorporated into its fractionation scheme.

Despite these examples that were congruent with our predictions, we observed a few exceptions in which the results did not agree with our initial hypotheses. The hand sensorimotor (Figure 4, Network 3) and mouth sensorimotor network (Network 9; associated with speech-motor processing (Laird et al., 2011a)), were observed in the high rather than moderate or low fractionation group. Similarly, the visual association network (Network 8) was observed to be highly fractionated, although at the low end of this group. Conversely, the left central executive network (Figure 5, Network 11), associated with language and memory tasks (Laird et al., 2011a), exhibited a moderate rather than high fractionation pattern. Most notably, the anterior and posterior default mode networks (Networks 16 and 14, respectively) demonstrated relatively simple fractionation patterns in comparison to other cognitive networks. Lastly, the self-referential network (Network 18; Mantini et al., 2007), associated with self-related (Northoff et al., 2006; Araujo et al., 2013; Andrews-Hanna et al., 2014), olfactory, gustatory, and affective processing (Laird et al., 2011a), exhibited no fractionation and was not observed to decompose into any child sub-networks as model order increased.

Given these exceptions, we considered other interpretations for the observed heterogeneity of network fractionation beyond a cognitive-motor-perceptual gradient. Comparison of the three groupings shown in Figures 4, 5, and 6 revealed that high fractionation networks were frequently localized to regions in the prefrontal cortex, suggesting that fractionation complexity may potentially evolve from primitive to more advanced networks. For example, Wey and colleagues (2014) examined resting state networks in fMRI data across four primate species, including humans, chimpanzees (a Great Ape), baboons (an Old World primate), and capuchin monkeys (a New World primate). Across all species, most networks were not lateralized to a single hemisphere, and the few networks exhibiting left and right asymmetries were present in both humans and non-human primates (NHP). In contrast, only humans displayed networks composed of both frontal and parietal nodes, whereas the frontal and parietal nodes were split into distinct networks among NHP. Thus, the notable difference between resting state networks in humans and NHP was multi-regional, *inter-lobar connectivity*. Importantly, inter-lobar fronto-parietal connectivity is exemplified by the dorsal attention and central executive networks, which are associated with higher-order cognitive processes. In light of these findings, an alternative and parsimonious explanation for the current results may lie in the evolutionary significance of multi-regional, inter-lobar connectivity, such that high fractionation networks are more widely distributed across the brain, whereas low fractionation networks are more localized within single lobes. The idea that stable networks correspond to networks with reduced connectivity in the context of ICA-derived fractionation has been proposed by others (Abou-Elseoud et al., 2010; Pamilo et al., 2012). Our present results generally agree with the distributed inter-lobar theory as an explanation for the significance underlying high-to-low network fractionation. Extensive inter-lobar coactivations were observed for the high fractionation networks, particularly across fronto-parietal regions. Inter-lobar coactivations were reduced in moderate fractionation networks, and low fractionation networks emphasized intra-lobar coactivations, particularly in medial regions. Indeed, the prominent difference in fractionation complexity for the right and left central executive network (Networks 1 and 11, respectively) may be explained by the extensive fronto-parietal coactivations of the highly fractionated network and the greater emphasis of intra-lobar coactivation (specifically in Broca's area) in the less fractionated network.

Nevertheless, an important outlier to this interpretation is the default mode network (DMN). This highly reproducible (Meindl et al., 2010) and heritable (Glahn et al., 2010) network is associated with spontaneous and non-goal-directed cognition during the resting state (Raichle et al., 2001; Buckner et al., 2008) and social cognition, self-monitoring, and episodic memory in the task state (Laird et al., 2009; Spreng et al., 2009). Given its long-range coactivations, we expected to observe extensive and complex fractionation of the DMN, particularly since it has been shown to exhibit heterogeneous network structure (Buckner et al., 2008; Harrison et al., 2008; Andrews-Hanna et al., 2010) well beyond the anterior and posterior subdivisions observed at low-model orders (Networks 16 and 14, respectively). However, the DMN demonstrated minimal fractionation, which potentially reflects a significant difference between meta-analytic task-based (Laird et al., 2009) and resting state network organization (Buckner et al., 2008; Harrison et al., 2008; Andrews-Hanna et al., 2010). That is, while during task DMN is involved in certain goal-directed behaviors with strong cognitive roles, the fundamental organization of the DMN cannot be captured during task but instead should rely on a combination of both task and resting state data for a more comprehensive assessment.

Methodological Considerations and Limitations

The meta-analytic approach for examining coactivation networks provides insight into functional brain organization across a wide range of goal-directed tasks. However, it is important to acknowledge the standard limitations that accompany large-scale mining of the BrainMap database. Working with pseudo-activation images derived from peak coordinates, rather than the whole brain statistical parametric images, diminishes the high spatial complexity and richness of the original maps and results in a loss of spatial sensitivity and specificity (Salimi-Khorshidi et al., 2009). In addition, spatial precision may be lost due to the variability of experimental parameters, such as scanner strength, imaging parameters, analysis pipelines, subject sample size, data quality, and variations in behavioral paradigm conditions. The functional decoding procedure is generally contingent on the design and implementation of BrainMap's metadata taxonomy, particularly for the behavioral domain field. These results are additionally dependent on the heterogeneity of experiments in the BrainMap database. There is an uneven distribution of experiments archived in BrainMap in which 49% of experiments elicit cognitive processes, 18% are emotion related processes, 16% of experiments are perception related, 15% are associated with action paradigms, and 2% with interoceptive experiments. Future work may involve expansion or refinement of the BrainMap taxonomy to ascertain if functional network differences can be discriminated at greater levels of resolution; current investigations into the utility of text-mining approaches for this purpose are ongoing (Turner et al., 2013). Prior work has demonstrated that the ICA approach reliably yields consistent component spatial maps (Ray et al., 2013), although that reliability is known to be reduced at higher model orders (Abou-Elseoud et al., 2010; Pamilo et al., 2013). As previously noted, the rationale for the combined approach of applying ICA followed by MACM was to address, in part, some of this variability and provide a more extensive and complete definition of the functional brain networks underlying each of the ICA component images. Initial testing of this approach revealed that the combined ICA-MACM method yielded similar results compared to ICA alone for model orders less than *d* = 100; however, more robust fractionation profiles were observed for the combined approach and this correspondence diminished as model order was increased up to *d* = 300.

Beyond these issues with data heterogeneity and reliability, generating multi-scale fractionation profiles via pair-wise correlations at consecutive model orders relied on a procedure that constrained the parent-child assignments to a static hierarchical structure that may or may not have captured all possible decomposition scenarios. For example, if a parent network at *d* = 30 was not matched to a child network at *d* = 40, then the *d* = 30 parent would not have any representation at *d* = 50 and beyond. As noted by Pamilo et al. (2012), fractionation profiles can be quite complex, and some decompositions may not include a single parent network splitting into two child sub-networks, but instead a merging of two or more parents. We attempted to address some of this complexity by allowing for children to be assigned to multiple parents, given a correlation difference within 0.01. We observed no evidence to suggest that if a parent network drops out of the analysis the subsequent children were forced to match with mismatched parents (i.e., that a network "skips a generation"). As an alternative to matching the *i+10* to *i* model order pairings, we initially investigated a procedure in which all children were matched to the *d* = 20 canonical networks. We observed that the resultant correlation assignments were prone to error as model order increased and sub-networks became progressively more differentiated from the canonical networks. Our approach of examining the *i+10* to *i* model order pairings was thus preferred as it highlighted incremental changes in network decomposition across model orders, thus providing a more interpretable continuum of fractionation. Concern that the increased power of the combined ICA-MACM approach (and larger extent of the MACM-based images) was simply blurring and conflating the differences between networks was mitigated by inspection of the child-parent assignments. As shown in the Supplemental Material, the probability of a child network being associated with multiple parent networks was observed to be quite low for the MACM-based results. In contrast, we found that assignment of child sub-networks to parent networks was more challenging when using the ICA component images, due to the additional noise in the fractionation patterns themselves as model order increased and the component size decreased.

Similarly, multiple approaches for computing similarity across model orders were considered, including the Dice index that has proven useful for examining spatial similarities in statistical parametric images exhibiting characteristic dependencies (Salimi-Khorshidi et al., 2009). After considering the different factors, we chose to perform the correlation analyses on the unthresholded meta-analytic *z*-statistic images that account for the different numbers of experiments contributing to the results, given that the MACM values scale strongly with it and thus provides the added value of assessing similarity between strength of network associated at a given spatial location. This procedure has been consistently applied in our recent work (c.f. Eickhoff et al., 2016; Ray et al., 2015; Bzdok et al., 2015), and was originally established by Eickhoff et al. (2011). Although this prior work has suggested that analysis of the unthresholded images is preferred over the thresholded images, a recent study (Sochat et al., 2015) demonstrated that thresholding may improve the accuracy of image similarity computations. In their study, Sochat et al. implemented a smaller degree of thresholding than what we have previously tested; therefore, our future work may evaluate such an approach.

Lastly, we acknowledge the limitations in extending the present work from task-based coactivation networks to resting state networks. Mennes et al. (2013) demonstrated that the complex relationship between intrinsic and extrinsic connectivity, revealing that evoked interaction patterns show weaker correspondence to intrinsic connectivity networks, particularly for subcortical and limbic regions, as well as primary sensorimotor areas. There is no substitute for the precision, temporal resolution, and power of a carefully controlled task-based neuroimaging experiment. With regards to the default mode network, we reiterate that the current results suggest that the functional organization of the DMN may not be captured by meta-analytic coactivation fractionation profiles, given the inherent differences between task and resting states.

Conclusions

The fractionation patterns of meta-analytic coactivation networks were observed to be highly heterogeneous and followed a tripartite model of high, moderate, and low fractionation. Functional decoding of coactivation networks revealed a multi-domain association regardless of fractionation complexity. Our initial prediction emphasizing a cognitive-motor-perceptual gradient from high to low fractionation was found to be true in many ways, with some notable exceptions. Further consideration of the results suggested an alternative interpretation that instead emphasized the importance of inter-lobar connectivity as a critical feature in the organization of human brain architecture. These outcomes suggest that high fractionation networks are complex and comprised of many constituent sub-networks reflecting long-range, inter-lobar connectivity, particularly in fronto-parietal regions. In contrast, low fractionation networks appear to reflect persistent and stable networks that are more internally coherent and exhibit less inter-lobar communication.

Acknowledgments

This work was supported by awards from the National Institute of Mental Health (R01-MH074457, R01-MH084812, and R56-MH097870) and the National Institute of Drug Abuse (K01-DA037819). Special thanks to Angela Uecker and Mick Fox of the University of Texas Health Science Center San Antonio for providing their BrainMap-related expertise.

References

Abou-Elseoud A, Starck T, Remes J, Nikkinen J, Tervonen O, Kiviniemi V. The effect of model order selection in group PICA. Hum Brain Mapp 31, 1207-1216, 2010.

Achard S, Salvador R, Whitcher B, Suckling J, Bullmore E. A resilient, low-frequency, small-world human brain functional network with highly connected association cortical hubs. J Neurosci 25, 63-72, 2006.

Andrews-Hanna JR, Reidler JS, Sepulcre J, Poulin R, Buckner RL. Functional-anatomic fractionation of the brain’s default network. Neuron 65, 550-562, 2010.

Andrews-Hanna JR, Saxe R, Yarkoni T. Contributions of episodic retrieval and mentalizing to autobiographical thought: evidence from functional neuroimaging, resting-state connectivity, and fMRI meta-analyses. Neuroimage 91, 324-335, 2014.

Allen EA, Erhardt EB, Damaraju E, Gruner W, Segall JM, Silva RF, Havlicek M, Rachakonda S, Fries J, Kalyanam R, Michael AM, Caprihan A, Turner JA, Eichele T, Adelsheim S, Bryan AD, Bustillo J, Clark VP, Feldstein Ewing SW, Filbey F, Ford CC, Hutchison K, Jung RE, Kiehl KA, Kodituwakku P, Komesu YM, Mayer AR, Pearlson GD, Phillips JP, Sadek JR, Stevens M, Teuscher U, Thoma RJ, Calhoun VD. A baseline for the multivariate comparison of resting state networks. Front Sys Neurosci 5, 2, 2011.

Araujo HF, Kaplan J, Damasio A. Cortical midline structures and autobiographical-self processes: an activation-likelihood estimation meta-analysis. Front Hum Neurosci 7, 548, 2013.

Bar M, Aminoff E, Schacter DL. Scenes unseen: The parahippocampal cortex intrinsically subserves contextual assocations, not scenes or places per se. J Neurosci 28, 8539-8544, 2008.

Baldassano C, Beck DM, Fei FL. Differential connectivity with the parahippocampal place area. Neuroimage 75, 236-245, 2013.

Beckmann CF, Smith SM. Probabilistic independent component analysis for functional magnetic resonance imaging. IEEE Trans. Med. Imaging 23, 137-152, 2004.

Beckmann CF, DeLuca M, Devlin JT, Smith SM. Investigations into resting-state connectivity using independent component analysis. Philos Trans R Soc Lond B Biol Sci 360, 1001-1013, 2005.

Beckmann CF. Modelling with independent components. NeuroImage 62, 891-901, 2012.

Biswal BB, Mennes M, Zuo XN, Gohel S, Kelly C, Smith SM, Beckmann CF, Adelstein JS, Buckner RL, Colcombe S, Dogonowski AM, Ernst M, Fair D, Hampson M, Hoptman MJ, Hyde JS, Kiviniemi VJ, Kötter R, Li SJ, Lin CP, Lowe MJ, Mackay C, Madden DJ, Madsen KH, Margulies DS, Mayberg HS, McMahon K, Monk CS, Mostofsky SH, Nagel BJ, Pekar JJ, Peltier SJ, Petersen SE, Riedl V, Rombouts SA, Rypma B, Schlaggar BL, Schmidt S, Seidler RD, Siegle GJ, Sorg C, Teng GJ, Veijola J, Villringer A, Walter M, Wang L, Weng XC, Whitfield-Gabrieli S, Williamson P, Windischberger C, Zang YF, Zhang HY, Castellanos FX, Milham MP. Toward discovery science of human brain function. Proc Natl Acad Sci 107, 4734-4739, 2010.

Bostock M, Ogievetsky V, Heer J. D^3 data-driven documents. IEEE Transactions on Visualization and Computer Graphics 17, 2301-2309, 2011.

Buckner RL, Andrews-Hanna JR, Schacter DL. The brain’s default network: Anatomy, function, and relevance to disease. Ann N Y Acad Sci 1124, 1-38, 2008.

Buckner RL, Sepulcre J, Talukdar T, Krienene FM, Liu H, Hedden T, Andrews-Hanna JR, Sperling RA, Johnson KA. Cortical hubs revealed by intrinsic functional connectivity: Mapping, assessment of stability, and relation to Alzheimer’s disease. J Neurosci 29, 1860-1873, 2009.

Bullmore E, Sporns O. Complex brain networks: Graph theoretical analysis of structural and functional systems. Nat Rev Neurosci 10, 186-198, 2009.

Bzdok D, Heeger A, Langner R, Laird AR, Fox PT, Palomero-Gallagher N, Vogt BA, Zilles K, Eickhoff SB. Subspecialization in the human posterior medial cortex. Neuroimage 106-55-71, 2015.

Calhoun VD, Adali T. Multisubject independent component analysis of fMRI: A decade of intrinsic networks, default mode, and neurodiagnostic discovery. IEEE Reviews in Biomedical Engineering 5, 60-73, 2012.

Chai XJ, Ofen N, Jacobs LF, Gabrieli JDE. Scene complexity: Influence on perception, memory, and development in the medial temporal lobe. Front Hum Neurosci 4, 21, 2010.

Cieslik EC, Zilles K, Caspers S, Roski C, Kellerman TS, Jakobs O, Langer R, Laird AR, Fox PT, Eickhoff SB. Is there “one” DLPFC in cognitive action control? Evidence for heterogeneity from co-activation-based parcellation. Cereb Cortex 23, 2677-2698, 2013.

Collins DL, Neelin P, Peters TM, Evans AC. Automatic 3D intersubject registration of MR volumetric data in standardized Talairach space. J Comput Assist Tomogr 18, 192-205, 1994.

Corbetta M, Shulman GL. Control of goal-directed and stimulus-driven attention in the brain. Nat Rev Neurosci 3, 201-215, 2002.

De Luca M, Beckmann CF, De Stefano N, Matthews PM, Smith SM. FMRI resting state networks define distinct modes of long-distance interactions in the human brain. Neuroimage 29, 1359-1367, 2006.

Damoiseaux JS, Rombouts SA, Barkhof F, Scheltens P, Stam CJ, Smith SM, Beckmann CF. Consistent resting-state networks across healthy subjects. Proc Natl Acad Sci USA 103, 13848-13853, 2006.

Ding JR, Liao W, Zhang Z, Mantini D, Xu Q, Wu GR, Lu G, Chen H. Topological fractionation of resting state networks. PLoS ONE 6, e26596, 2011.

Dobromyslin VI, Salat DH, Fortier CB, Beckmann CV, Milberg WP, McGlinchey RE. Distinct functional networks within the cerebellum and their relation to cortical systems assessed with independent component analysis. Neuroimage 60, 2073-2085, 2012.

Dosenbach NUF, Visscher KM, Palmer ED, Miezin FM, Wenger KK, Kang HC, Burgund ED, Grimes AL, Schlagger BL, Petersen SE. A core system for the implementation of task sets. Neuron 50, 799-812, 2006.

Eickhoff SB, Laird AR, Grefkes C, Wang LE, Zilles K, Fox PT. Coordinate-based activation likelihood estimation meta-analysis of neuroimaging data: A random-effects approach based on empirical estimates of spatial uncertainty. Hum Brain Mapp 30, 2907-2926, 2009.

Eickhoff S, Jbabdi S, Caspers S, Laird AR, Fox PT, Zilles K, Behrens T. Anatomical and functional connectivity of cytoarchitectonic areas within the human parietal operculum. J Neurosci 30, 6409-6421, 2010.

Eickhoff SB, Bzdok D, Laird AR, Roski C, Caspers S, Zilles K, Fox PT. Co-activation patterns distinguish cortical modules, their connectivity and functional differentiation. Neuroimage 57, 938-949, 2011.

Eickhoff SB, Bzdok D, Laird AR, Kurth F, Fox PT. Activation likelihood estimation revisited. Neuroimage 59, 2349-2361, 2012.

Eickhoff SB, Laird AR, Fox PT, Bzdok D, Hensel L. Functional segregation of the human dorsomedial prefrontal cortex. Cereb Cortex 304-321, 2016.

Evans AC, Collins DL, Mills SR, Brown ED, Kelly RL, Peters TM. 3D statistical neuroanatomical models from 305 MRI volumes. Proceedings of IEEE-Nuclear Science Symposium and Medical Imaging Conference, 1813–1817, 1993.

Fox PT, Lancaster JL. Mapping context and content: The BrainMap model. Nature Rev Neurosci 3, 319-321, 2002.

Fox PT, Laird AR, Fox SP, Fox PM, Uecker AM, Crank M, Koenig SF, Lancaster JL. BrainMap taxonomy of experimental design: Description and evaluation. Hum Brain Mapp 25, 185-198, 2005.

Fox MD, Corbetta M, Snyder AZ, Vincent JL, Raichle ME. Spontaneous neuronal activity distinguishes human dorsal and ventral attention systems. Proc Natl Acad Sci USA 103, 100046-100051, 2006.

Glahn DC, Winkler AM, Kochunov P, Almasy L, Duggirala R, Carless MA, Curran JC, Olvera RL, Laird AR, Smith SM, Beckmann CF, Fox PT, Blangero J. Genetic control over the resting brain. Proc Natl Acad Sci USA 107, 1223-1228, 2010.

Hagmann P, Cammoun L, Gigandet X, Meuli R, Honey CJ, Wedeen VJ, Sporns O. Mapping the structural core of human cerebral cortex. PLoS Biol 6, e159, 2008.

Harrison BJ, Pujol J, López-Solà M, Hernández-Ribas R, Deus J, Ortiz H, Soriano-Mas C, Yücel M, Pantelis C, Cardoner N. Consistency and functional specialization in the default mode brain network. Proc Natl Acad Sci USA 105, 9781-9786, 2008.

He Y, Wang J, Wang L, Chen ZJ, Yan C, Yang H, Tang H, Zhu C, Gong Q, Zang Y, Evans AC. Uncovering intrinsic modular organization of spontaneous brain activity in humans. PLoS ONE 4, e5226, 2009.

Henderson JM, Larson CL, Zhu CD. Cortical activation to indoor versus outdoor scenes: An fMRI study. Exp Brain Res 179, 75-84, 2007.

Himberg J, Hyvärinen A, Esposito F. Validating the independent components of neuroimaging time series via clustering and visualization. Neuroimage 22, 1214–1222, 2004.

Jakobs O, Langner R, Caspers S, Roski C, Cieslik EC, Zilles K, Laird AR, Fox PT, Eickhoff SB. Across-study and within-subject functional connectivity of a right temporo-parietal junction subregion involved in stimulus-context integration. Neuroimage 60, 2389-2398, 2012.

Jenkinson M, Beckmann CF, Behrens TEJ, Woolrich MW, Smith SM. FSL. Neuroimage 62, 782–790, 2012.

Kim DJ, Park B, Park HJ. Functional connectivity-based identification of subdivisions of the basal ganglia and thalamus using multilevel independent component analysis of resting state fMRI. Hum Brain Mapp 34, 1371-1385, 2013.

Kiviniemi V, Starck T, Remes J, Long X, Nikkinen J, Haapea M, Veijola J, Moilanen I, Isohanni M, Zang YF, Tervonen O. Functional segmentation of the brain cortex using high model order group PICA. Hum Brain Mapp 30, 3865-3886, 2009.

Kochunov P, Lancaster J, Thompson P, Toga AW, Brewer P, Hardies J, Fox P. An optimized individual target brain in the Talairach coordinate system. Neuroimage 17, 922-927, 2002.

Laird AR, Lancaster JL, Fox PT. BrainMap: The social evolution of a functional neuroimaging database. Neuroinformatics 3, 65-78, 2005a.

Laird AR, Fox M, Price CJ, Glahn DC, Uecker AM, Lancaster JL, Turkeltaub PE, Kochunov P, Fox PT. ALE meta-analysis: Controlling the false discovery rate and performing statistical contrasts. Hum Brain Mapp 25, 155-164, 2005b.

Laird AR, Eickhoff SB, Li K, Robin DA, Glahn DC, Fox PT. Investigating the functional heterogeneity of the default mode network using coordinate-based meta-analytic modeling. J Neurosci 29, 14496-14505, 2009a.

Laird AR, Eickhoff SB, Kurth F, Fox PM, Uecker AM, Turner JA, Robinson JL, Lancaster JL, Fox PT. ALE meta-analysis workflows via the BrainMap database: Progress towards a probabilistic functional brain atlas. Front Neuroinform 3, 2009b.

Laird AR, Robinson JL, McMillan KM, Tordesillas-Gutierrez D, Moran ST, Ray KL, Franklin C, Glahn DC, Fox PT, Lancaster JL. Comparison of the disparity between Talairach and MNI coordinates in functional neuroimaging data: Validation of the Lancaster transform. Neuroimage 51, 677-683, 2010.

Laird AR, Fox PM, Eickhoff SB, Turner JA, Ray KL, McKay DR, Glahn DC, Beckmann CF, Smith SM, Fox PT. Behavioral interpretations of intrinsic connectivity networks. J Cogn Neurosci 23, 4022-37, 2011a.

Laird AR, Eickhoff SB, Fox PM, Uecker AM, Ray KL, Saenz JJ, McKay DR, Bzdok D, Laird RW, Robinson JL, Turner JA, Turkeltaub PE, Lancaster JL, Fox PT. The BrainMap strategy for standardization, sharing, and meta-analysis of neuroimaging data. BMC Res Notes 4, 349, 2011b.

Laird AR, Riedel MC, Sutherland MT, Eickhoff SB, Ray KL, Uecker AM, Fox PM, Turner JA, Fox PT. Neural architecture underlying classification of face perception paradigms. Neuroimage 119, 70-80, 2015.

Lancaster JL, Tordesillas-Gutiérrez D, Martinez M, Salinas F, Evans A, Zilles K, Mazziotta JC, Fox PT. Bias between MNI and Talairach coordinates analyzed using the ICBM-152 brain template. Hum Brain Mapp 28, 1194-1205, 2007.

Land MF. Do we have an internal model of the outside world? Philos Trans R Soc Lond B Biol Sci 369, 20130045, 2014.

Lester BD, Dassonville P. The role of the right superior parietal lobule in processing visual context for the establishment of the egocentric reference frame. J Cogn Neurosci 26, 2201-2209, 2014.

Li Y, Adali T, Calhoun VD. Estimating the number of independent components for functional magnetic resonance imaging data. Hum Brain Mapp 28, 1251-1266, 2007.

Mantini D, Perrucci MG, Del Gratta C, Romani GL, Corbetta M. Electrophysiological signatures of resting state networks in the human brain. Proc Natl Acad Sci USA 104, 13170-13175, 2007.

Meindl T, Teipel S, Elmouden R, Mueller S, Koch W, Dietrich O, Coates U, Reiser M. Test-retest reproducibility of the default mode network in healthy individuals. Hum Brain Mapp 31, 237-246, 2010.
Mennes M, Kelly C, Colcombe S, Castellanos FX, Milham MP. The extrinsic and intrinsic functional architectures of the human brain are not equivalent. Cerebral Cortex 23, 223-229, 2013.
Menon V, Uddin LQ. Saliency, switching, attention, and control: A network model of insula function. Brain Struct Funct 214, 655-667, 2010.

Meunier D, Lambiotte, R, Fornito A, Ersche KD, Bullmore ET. Hierarchical modularity in human brain functional networks. Front Neuroinform 3, 37, 2009.

Moeller S, Nallasamy N, Tsao DY, Freiwald WA. Functional connectivity of the macaque brain across stimulus and arousal states. J Neurosci 29, 5897-5909, 2009.

Narayana S, Laird AR, Tandon N, Franklin C, Lancaster JL, Fox PT. Electrophysiological and functional connectivity of the human supplementary motor area. Neuroimage 62, 250-265, 2012.

Nickl-Jockschat T, Rottschy C, Thommes J, Schneider F, Laird AR, Fox PT, Eickhoff SB. Neural networks related to dysfunctional face processing in autism spectrum disorder. Brain Struct Funct 220, 2355-2371, 2015.

Northoff G, Heinzel A, de Greck M, Bermpohl F, Dobrowolny H, Panksepp J. Self-referential processing in our brain--a meta-analysis of imaging studies on the self. Neuroimage 31, 440-457, 2006.

Pamilo S, Malinen S, Hlushchuk Y, Seppa M, Tikka P, Hari R. Functional subdivision of group-ICA results of fMRI data collected during cinema viewing. PLoS ONE 7, e42000, 2012.

Parkinson A, Condon L, Jackson SR. Parietal cortex coding of limb posture: In search of the body-schema. Neuropsychologia 48, 3228-3234, 2010.

Poldrack RA. Can cognitive processes be inferred from neuroimaging data? Trends Cogn Sci 10, 59-63, 2006.

Raichle ME, MacLeod AM, Snyder AZ, Powers WJ, Gusnard DA, Shulman GL. A default mode of brain function. Proc Natl Acad Sci USA 98, 676-682, 2001.

Ray KL, McKay DR, Fox PM, Riedel MC, Uecker AM, Beckmann CF, Smith SM, Fox PT, Laird AR. ICA model order selection of task co-activation networks. Front Neurosci 7, 237, 2013.

Ray KL, Zald DH, Bludau S, Riedel MC, Bzdok D, Yanes J, Falcone KE, Amunts K, Fox PT, Eickhoff SB, Laird AR. Co-activation based parcellation of the human frontal pole. Neuroimage 123, 200-211, 2015.

Reetz K, Dogan I, Rolfs A, Binkofski F, Schulz JB, Laird AR, Fox PT, Eickhoff SB. Investigating function and connectivity of morphometric findings--exemplified on cerebellar atrophy in spinocerebellar ataxia 17 (SCA17). Neuroimage 62, 1354-1366, 2012.

Riedel MC, Ray KL, Dick AS, Sutherland MT, Hernandez Z, Fox PM, Eickhoff SB, Fox PT, Laird AR. Meta-analytic connectivity and behavioral parcellation of the human cerebellum. Neuroimage 117, 327-342, 2015.

Robinson S, Basso G, Soldati N, Sailer U, Jovicich J, Bruzzone L, Kryspin-Exner I, Bauer H, Moser E. A resting state network in the motor control circuit of the basal ganglia. BMC Neurosci 10, 137, 2009.

Robinson JL, Laird AR, Glahn DC, Lovallo WR, Fox PT. Meta-analytic connectivity modelling: Delineating the functional connectivity of the human amygdala. Hum Brain Mapp 31, 173-184, 2010.

Robinson JL, Laird AR, Glahn DC, Blangero J, Sanghera MK, Pessoa L, Fox PM, Uecker A, Friehs G, Young KA, Griffin JL, Lovallo WR, Fox PT. The functional connectivity of the human caudate: an application of meta-analytic connectivity modeling with behavioral filtering. Neuroimage 60, 117-129, 2012.

Salimi-Khorshidi G, Smith SM, Keltner JR, Wager TD, Nichols TE. Meta-analysis of neuroimaging data: A comparison of image-based and coordinate-based pooling of studies. Neuroimage 45, 810-823, 2009.

Salvador R, Suckling J Coleman MR, Pickard JD, Menon D, Bullmore E. Neurophysiological architecture of functional magnetic resonance images of human brain. Cereb Cortex 15, 1332-1342, 2005.

Scheperjans F, Grefkes C, Palomero-Gallagher N, Schleicher A, Zilles K. Subdivisions of human parietal area 5 revealed by quantitative receptor autoradiography: A parietal region between motor, somatosensory, and cingulate cortical areas. Neuroimage 25, 975-992, 2005.

Seeley WW, Menon V, Schatzberg AF, Keller J, Glover GH, Kenna H, Reiss AL, Greicius MD. Dissociable intrinsic connectivity networks for salience processing and executive control. J Neurosci 27, 2349-2356, 2007.

Seifritz E, Esposito F, Hennel F, Mustovic H, Neuhoff JG, Bilecen D, Tedeschi G, Scheffler K, Di Salle F. Spatiotemporal pattern of neural processing in the human auditory cortex. Science 297, 1706-1708, 2002.

Shannon P, Markiel A, Ozier O, Baliga NS, Wang JT, Ramage D, Amin N, Schwikowski B, Ideker T. Cytoscape: A software environment for integrated models of biomolecular interaction networks. Genome Res 13, 2498-2504, 2003.

Smith SM, Jenkinson M, Woolrich MW, Beckmann CF, Behrens TEJ, Johansen-Berg H, Bannister PR, De Luca M, Drobnjak I, Flitney DE, Niazy R, Saunders J, Vickers J, Zhang Y, De Stefano N, Brady JM, Matthews PM. Advances in functional and structural MR image analysis and implementation as FSL. Neuroimage 23, 208-219, 2004.

Smith SM, Fox PT, Miller KL, Glahn DC, Fox PM, Mackay CE, Filippini N, Watkins KE, Toro R, Laird AR, Beckmann CF. Correspondence of the brain's functional architecture during activation and rest. Proc Natl Acad Sci USA 106, 13040-13045, 2009.

Sochat VV, Gorgolewski KJ, Koyejo O, Durnez J, Poldrack RA. Effects of thresholding on correlation-based image similarity metrics. Front Neurosci 9, 418, 2015.

Spreng RN, Mar RA, Kim ASN. The common neural basis of autobiographical memory, prospection, navigation, theory of mind, and the default mode: A quantitative meta-analysis. J Cogn Neurosci 21, 489-510, 2009.

Sridharan D, Levitin DJ, Menon V. A critical role for the right fronto-insular cortex in switching between central-executive and default-mode networks. Proc Natl Acad Sci USA 105, 12569-12574, 2008.

Sulpizio V, Committeri G, Lambrey S, Berthoz A, Gaspare G. Selective role of lingual/parahippocampal gyrus and retrosplenial complex in spatial memory across viewpoint changes relative to the environmental reference frame. Behav Brain Res 242, 62-75, 2013.

Talairach J, Tournoux P. Co-planar stereotaxic atlas of the human brain. Thieme Medical Publishers, New York, 1988.

Turkeltaub PE, Eden GF, Jones KM, Zeffiro TA. Meta-analysis of the functional neuroanatomy of single-word reading: Method and validation. Neuroimage 16, 765-80, 2002.

Turkeltaub PE, Eickhoff SB, Laird AR, Fox PM, Wiener M, Fox PT. Minimizing within-experiment and within-group effects in activation likelihood estimation meta-analyses. Hum Brain Mapp 33, 1-13, 2012.

Turner MD, Chakrabarti C, Jones TB, Xu JF, Fox PT, Luger GF, Laird AR, Turner JA. Automated annotation of functional imaging experiments via multi-label classification. Front Neurosci 7, 240, 2013.

Vincent JL, Patel GH, Fox MD, Snyder AZ, Baker JT, Van Essen DC, Zempel JM, Snyder LH, Corbetta M, Raichle ME. Intrinsic functional architecture in the anaesthetized monkey brain. Nature 447, 83-86, 2007.

Vincent JL, Kahn I, Snyder AZ, Raichle ME, Buckner RL. Evidence for a frontoparietal control system revealed by intrinsic functional connectivity. J Neurophysiol 100, 3328-3342, 2008.

Wang Y, Li TQ. Dimensionality of ICA in resting-state fMRI investigated by feature optimized classification of independent components with SVM. Front Hum Neurosci 9, 259, 2015.

Wey HY, Phillips KA, McKay DR, Laird AR, Kochunov P, Davis MD, Glahn DC, Duong TQ, Fox PT. Multi-region hemispheric specialization differentiates human from nonhuman primate brain function. Brain Struct Funct 219, 2187-2194, 2014.

Wisner KM, Atluri G, Lim KO, MacDonald III AW. Neurometrics of intrinsic connectivity networks at rest using fMRI: Retest reliability and cross-validation using a meta-level method. Neuroimage 76, 236-251, 2013.

Woolrich MW, Jbabdi S, Patenaude B, Chappell M, Makni S, Behrens T, Beckmann C, Jenkinson M, Smith SM. Bayesian analysis of neuroimaging data in FSL. Neuroimage 45, S173-S186, 2009.

Yarkoni T, Poldrack RA, Nichols TE, Van Essen DC, Wager TD. Large-scale automated synthesis of human functional neuroimaging data. Nat Methods 8, 665-670, 2011.

Zuo XN, Kelly C, Adelstein JS, Klein DF, Castellanos FX, Milham MP. Reliable intrinsic connectivity networks: Test-retest evaluation using ICA and dual regression approach. Neuroimage 49, 2163-2177, 2010.

Figure Captions

Figure 1. Data Analysis Pipeline. Step 1: Per-experiment coordinate-based data were extracted from BrainMap and used to generate 10,899 modeled activation (MA) maps. Step 2: Independent component analysis was performed at a model order *d* to obtain component images. Step 3: MACM was performed on the ICA component images to identify the meta-analytic coactivation networks. Steps 2-3 were repeated $t = 29$ times for model orders $d = 20$ to 300 in intervals of 10. Step 4: Correlation coefficients were iteratively computed between consecutive model order pairs to establish parent-child sub-network assignments. Step 5: Hierarchical clustering analysis was performed on the family of sub-networks for each of the $d = 20$ canonical coactivation networks to identify groupings of networks with fractionation profiles of similar complexity.

Figure 2. Comparative Volume of ICA Component Images and MACM-Based Coactivation Networks. For the ICA spatial components, the average number of significant voxels ($z > 4$) per component exhibited a logarithmic decrease with model order ($R^2 = 0.972$), whereas for the MACM-based coactivation networks, the average number of significant voxels per MACM exhibited a linear decrease with model order ($R^2 = 0.977$). As model order increased, both sets of images exhibited a shift from broadly distributed networks encompassing multiple brain regions to more localized and discrete individual nodes.

Figure 3. Heterogeneity of Fractionation Profiles. The number of child sub-networks observed for each of the canonical coactivation networks was plotted as a function of model order. Hierarchical clustering of these data (inset) demonstrated three groupings of similar fractionation profiles: high fractionation, moderate fractionation, and low fractionation.

Figure 4. High Fractionation Networks. Clustering revealed a group of seven canonical networks with complex fractionation profiles exhibiting the highest degree of decomposition, shown in order of decreasing number of child sub-networks. High fractionation networks included (from left to right): (1) right-lateralized central executive network, (2) dorsal attention network, (3) hand sensorimotor network, (4) cerebellar network, (5) salience network, (6) basal ganglia and thalamus network, (7) visuomotor coordination network, (8) visual association network, and (9) mouth sensorimotor network. Upper row: meta-analytic coactivation networks; middle row: fractionation profiles; bottom row: behavioral profiles.

Figure 5. Moderate Fractionation Networks. Clustering revealed a group of six canonical networks with moderate fractionation profiles exhibiting less complexity and branching compared to the high fractionation group, shown in order of decreasing number of child sub-networks. Moderate fractionation networks included (from left to right): (10) lateral visual network, (11) left-lateralized central executive network, and (12) temporo-limbic network. Upper row: meta-analytic coactivation networks; middle row: fractionation profiles; bottom row: behavioral profiles.

Figure 6. Low Fractionation Networks. Clustering revealed a group of six canonical networks with low fractionation profiles exhibiting little to no decomposition, shown in order of decreasing number of child sub-networks. Low fractionation networks included (from left to right): (13) auditory network, (14) posterior default mode network, (15) medial visual network, (16) anterior default mode network, (17) contextual association network, (18) self-referential network, and (19) posterior association network. Upper row: meta-analytic coactivation networks; middle row: fractionation profiles; bottom row: behavioral profiles.

Figures

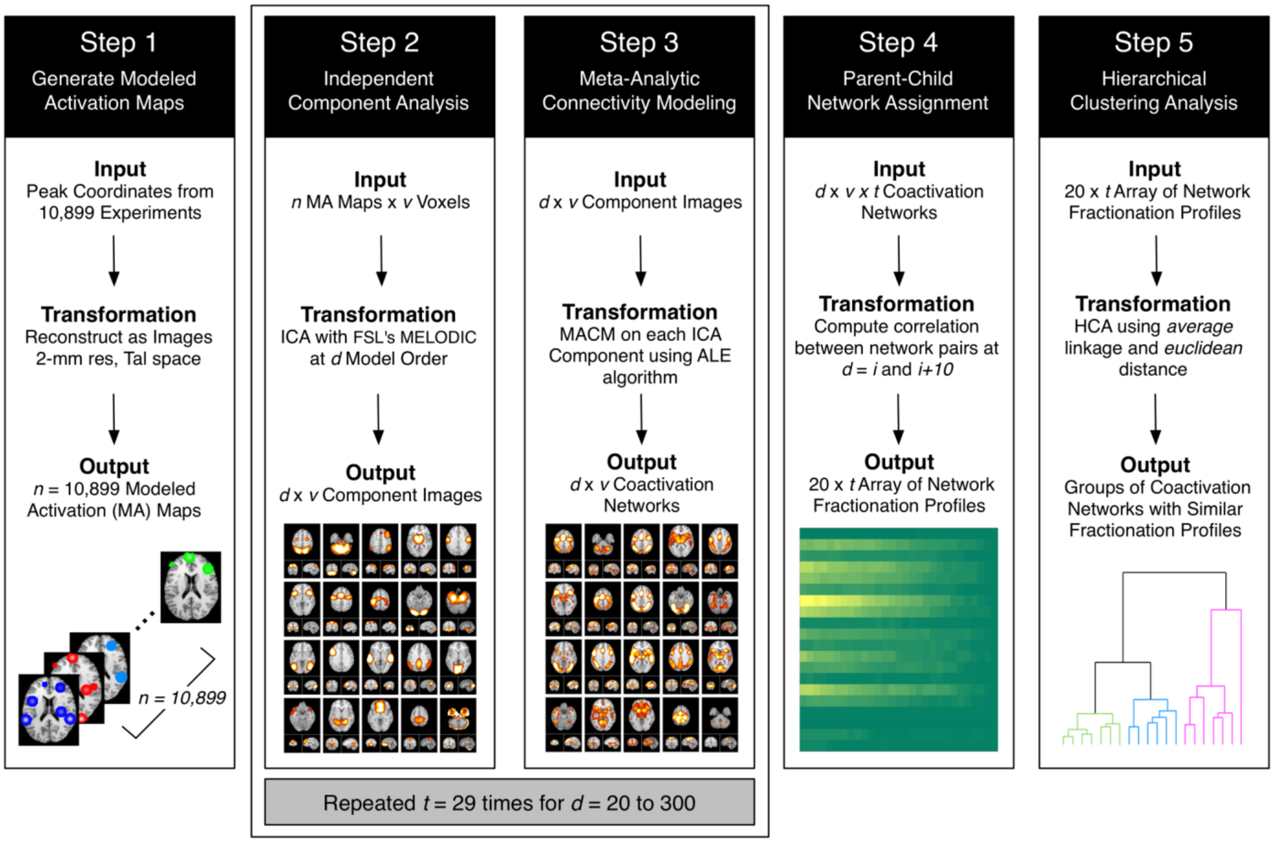

Figure 1. Data Analysis Pipeline.

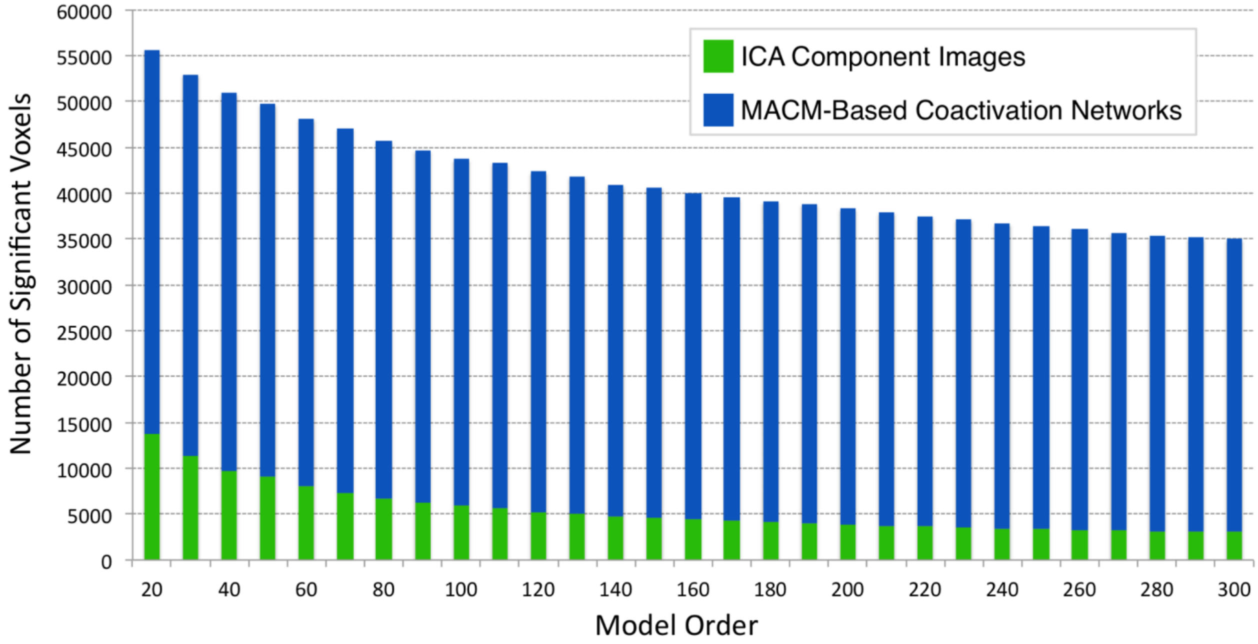

Figure 2. Comparative Volume of ICA Component Images and MACM-Based Coactivation Networks.

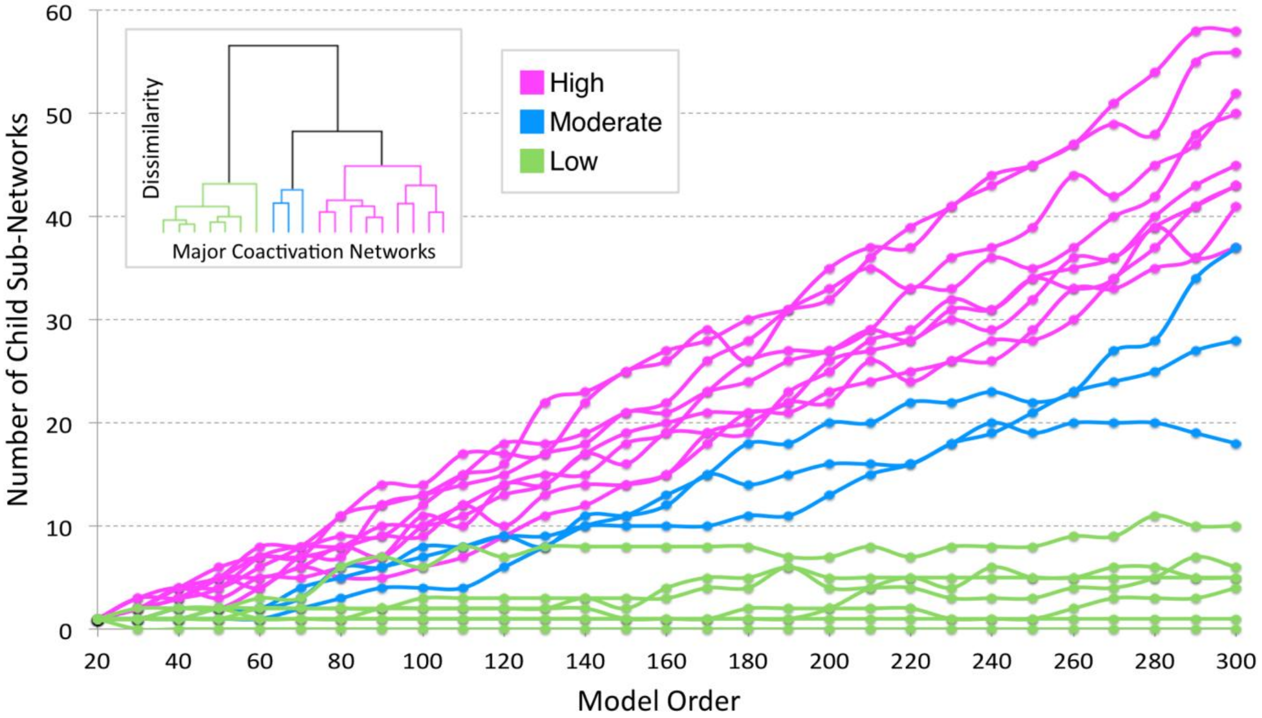

Figure 3. Heterogeneity of Fractionation Profiles.

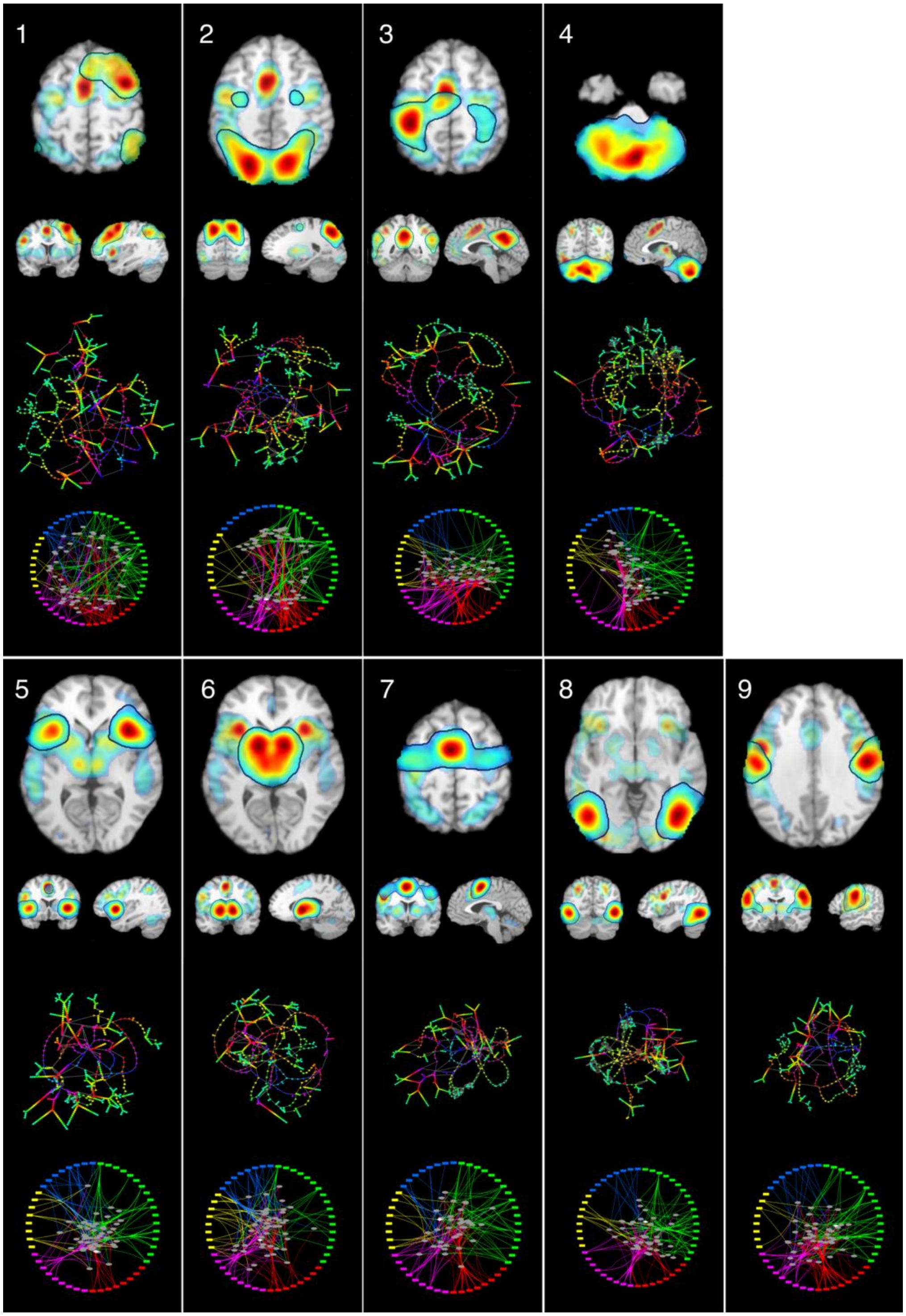

Figure 4. High Fractionation Networks.

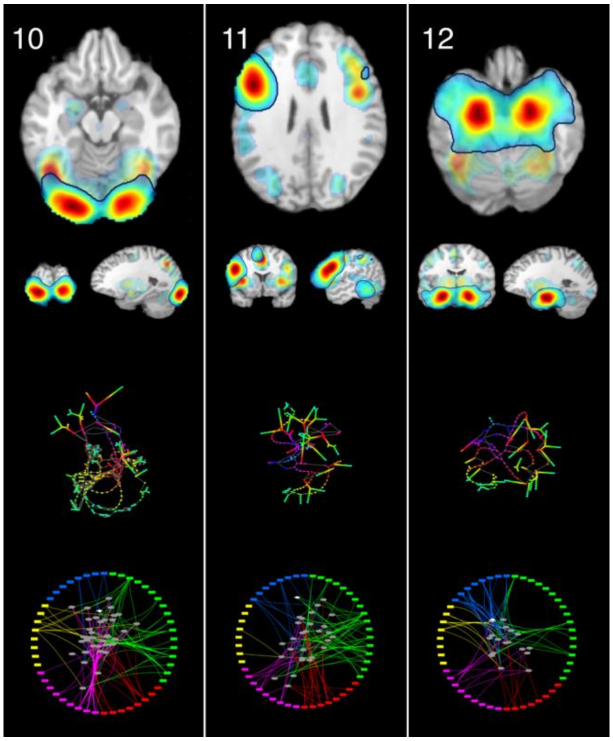

Figure 5. Moderate Fractionation Networks.

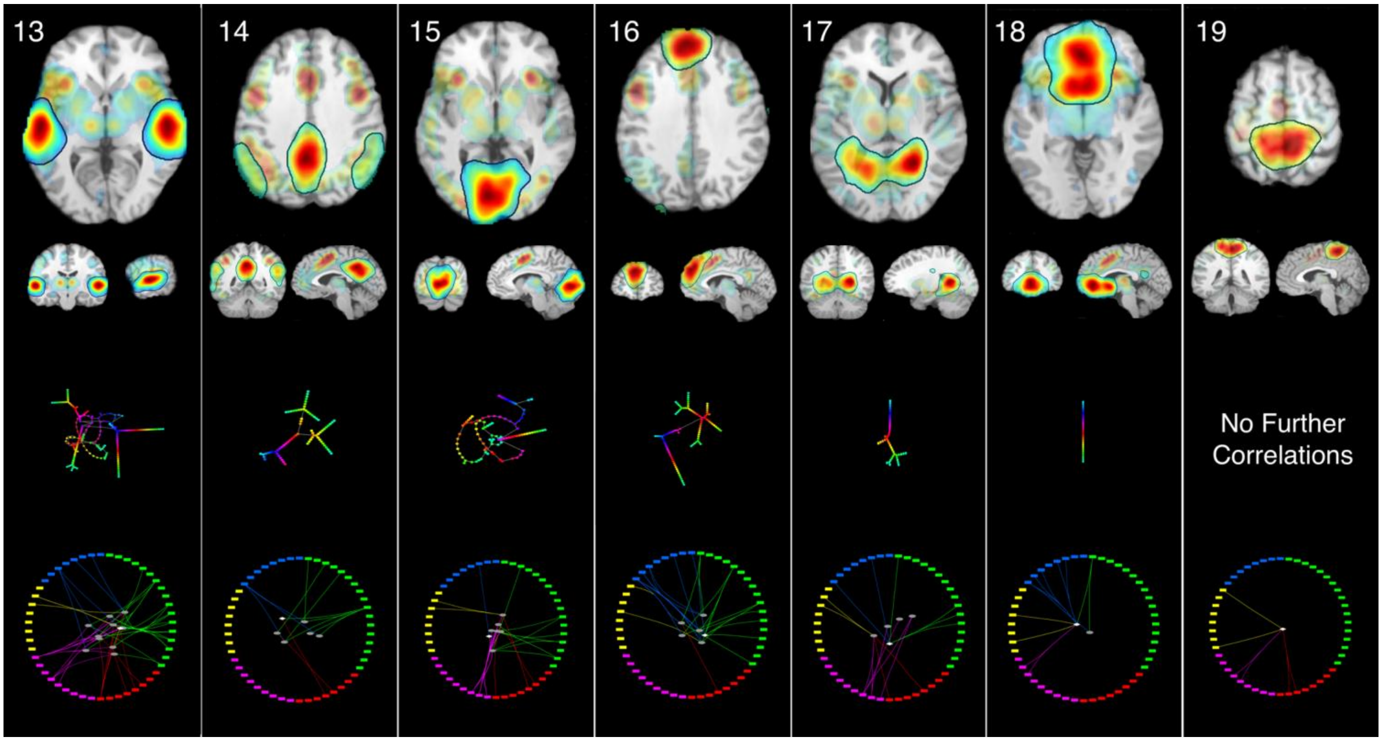

Figure 6. Low Fractionation Networks.

10. Supplementary Material